Eight new luminous $z \geq 6$ quasars discovered via SED model fitting of VISTA, *WISE* and Dark Energy Survey Year 1 observations

S. L. Reed,[1,2]★ R. G. McMahon,[1,2] P. Martini,[3,4] M. Banerji,[1,2] M. Auger,[1]
P. C. Hewett,[1] S. E. Koposov,[1] S. L. J. Gibbons,[1] E. Gonzalez-Solares,[1]
F. Ostrovski,[1,2] S. S. Tie,[3,4] F. B. Abdalla,[5,6] S. Allam,[7] A. Benoit-Lévy,[7,8,9]
E. Bertin,[8,9] D. Brooks,[5] E. Buckley-Geer,[7] D. L. Burke,[10,11] A. Carnero Rosell,[12,13]
M. Carrasco Kind,[14,15] J. Carretero,[16,17] L. N. da Costa,[12,13] D. L. DePoy,[18]
S. Desai,[19] H. T. Diehl,[7] P. Doel,[5] A. E. Evrard,[20,21] D. A. Finley,[7] B. Flaugher,[7]
P. Fosalba,[16] J. Frieman,[7,22] J. García-Bellido,[23] E. Gaztanaga,[16] D. A. Goldstein,[24,25]
D. Gruen,[11,26] R. A. Gruendl,[27,28] G. Gutierrez,[7] D. J. James,[29,30] K. Kuehn,[31]
N. Kuropatkin,[7] O. Lahav,[5] M. Lima,[12,32] M. A. G. Maia,[12,13] J. L. Marshall,[18]
P. Melchior,[33] C. J. Miller,[20,21] R. Miquel,[17,34] B. Nord,[7] R. Ogando,[12,13]
A. A. Plazas,[35] A. K. Romer,[36] E. Sanchez,[37] V. Scarpine,[7] M. Schubnell,[21]
I. Sevilla-Noarbe,[37] R. C. Smith,[30] F. Sobreira,[12,38] E. Suchyta,[39] M. E. C. Swanson,[28]
G. Tarle,[21] D. L. Tucker,[7] A. R. Walker[30] and W. Wester[7]

Affiliations are listed at the end of the paper

ABSTRACT

We present the discovery and spectroscopic confirmation with the European Southern Observatory New Technology Telescope (NTT) and Gemini South telescopes of eight new, and the rediscovery of two previously known, $6.0 < z < 6.5$ quasars with $z_{AB} < 21.0$. These quasars were photometrically selected without any morphological criteria from 1533 deg^2 using spectral energy distribution (SED) model fitting to photometric data from Dark Energy Survey (g, r, i, z, Y), VISTA Hemisphere Survey (J, H, K) and *Wide-field Infrared Survey Explorer* (*W1*, *W2*). The photometric data were fitted with a grid of quasar model SEDs with redshift-dependent Ly α forest absorption and a range of intrinsic reddening as well as a series of low-mass cool star models. Candidates were ranked using an SED-model-based χ^2-statistic, which is extendable to other future imaging surveys (e.g. LSST and Euclid). Our spectral confirmation success rate is 100 per cent without the need for follow-up photometric observations as used in other studies of this type. Combined with automatic removal of the main types of non-astrophysical contaminants, the method allows large data sets to be processed without human intervention and without being overrun by spurious false candidates. We also present a robust parametric redshift estimator that gives comparable accuracy to Mg II and CO-based redshift estimators. We find two $z \sim 6.2$ quasars with H II near zone sizes ≤ 3 proper Mpc that could indicate that these quasars may be young with ages $\lesssim 10^6 - 10^7$ years or lie in over dense regions of the IGM. The $z = 6.5$ quasar VDES J0224−4711 has $J_{AB} = 19.75$ and is the second most luminous quasar known with $z \geq 6.5$.

Key words: galaxies: active – galaxies: formation – galaxies: high redshift – quasars individual: VDES J0224−4711 – dark ages, reionization, first stars.

* E-mail: sr525@ast.cam.ac.uk

1 INTRODUCTION

Quasars are some of the most luminous sources in the high-redshift Universe and can be used as direct probes of very early times when the first generations of galaxies and quasars were forming. Their spectra can be used to throw light on the properties of the inter-galactic medium (IGM) as well as to give direct measurements of the neutral hydrogen fraction at the end of reionization through the study of Ly α forest absorption (Fan et al. 2006; Bolton & Haehnelt 2007). Absorption lines in the spectra of high-redshift quasars allow the properties of gas and metals to be studied on cosmological scales.

The results from the Cosmic Microwave Background (CMB) measurements given in Planck Collaboration XIII (2015) suggest that the beginning of reionization was at $z \sim 8$. At lower redshifts ($2.0 < z < 6.0$), studies (Gunn & Peterson 1965; Fan et al. 2006; Becker, Rauch & Sargent 2007) show that the IGM is highly ionized ($n_{\mathrm{H\,I}}/n_{\mathrm{H}} \leq 10^{-4}$) and therefore that reionization was complete by $z \sim 6$. The discovery of more quasars above a redshift of $z = 6$ will allow the change in hydrogen ionization at $z > 6$ to be studied in more detail and along different lines of sight.

There have been many surveys for high-redshift quasars and these have led to the discovery of ~ 60 quasars at $z > 6.0$ (e.g. Fan et al. 2006; Jiang et al. 2009, 2016; Willott et al. 2010; Mortlock et al. 2012; Venemans et al. 2013, 2015b; Carnall et al. 2015; Bañados et al. 2016). Most of these searches have used purely optical photometry from large surveys such as the Sloan Digital Sky Survey (SDSS) or the Canada–France–Hawaii Telescope Legacy Survey (CFHTLS) that have a reddest photometric wave-band of *z*. The deeper and redder photometry extending to the *Y* photometric waveband provided by the Dark Energy Survey (DES; The Dark Energy Survey Collaboration 2005) combined with the additional IR data from complementary surveys such as the VISTA Hemisphere Survey (VHS; McMahon et al. 2013) and the *Wide-field Infrared Survey Explorer* (*WISE*) means that samples can be cleanly selected without the need for deep photometric follow-up such as in Reed et al. (2015, hereafter R15). Infrared data are a powerful discriminant between high-redshift quasars and their main astrophysical contaminants of ultra-cool stars (Wright et al. 2010; Banerji et al. 2015).

The red sensitive Dark Energy Camera (DECam) CCD detectors, coupled with the long wavelength sensitivity of the DES *z* and *Y* filters, allow the detection of Ly α to higher redshift than was possible with less red sensitive optical surveys such as SDSS and increases the redshift range that can be covered to $z \sim 7$. In this paper, we present the results of our search for high-redshift quasars in the first year of DES data.

DES magnitudes, near-infrared (NIR) VISTA magnitudes and *WISE* magnitudes, are quoted on the AB system. The conversions from Vega to AB that have been used for the VISTA data are $J_{\mathrm{AB}} = J_{\mathrm{Vega}} + 0.937$ and $Ks_{\mathrm{AB}} = Ks_{\mathrm{Vega}} + 1.839$; these are taken from the Cambridge Astronomical Survey Unit's website.[1] The conversions used for the ALLWISE data are $W1_{\mathrm{AB}} = W1_{\mathrm{Vega}} + 2.699$ and $W2_{\mathrm{AB}} = W2_{\mathrm{Vega}} + 3.339$, which are given in Jarrett et al. (2011) and in the ALLWISE explanatory supplement.[2] When required, a

[1] http://casu.ast.cam.ac.uk/surveys-projects/vista/technical/filter-set
[2] The ALLWISE explanatory supplement, http://wise2.ipac.caltech.edu/docs/release/allwise/expsup/sec5_3e.html, directs the reader to the *WISE All-Sky* explanatory supplement for the conversions; http://wise2.ipac.caltech.edu/docs/release/allsky/expsup/sec4_4h.html#summary.
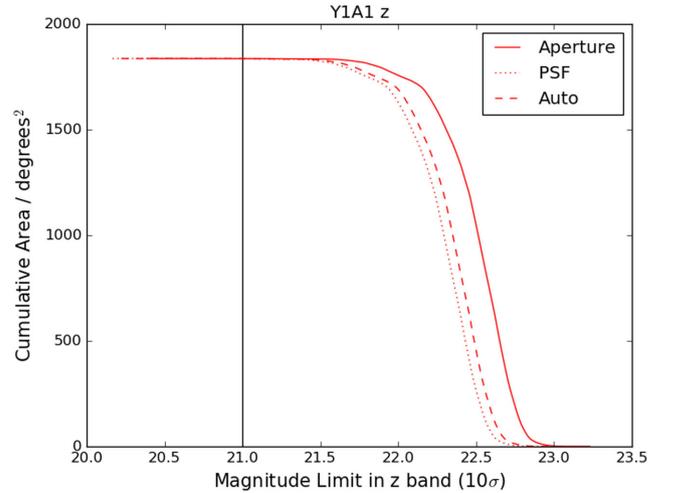
Figure 1. Cumulative area versus 10σ *z*-band depth in a 2 arcsec diameter aperture (solid line), PSF magnitudes (dotted line) and auto-magnitudes (dashed line) for the DES Y1A1 data. The aperture magnitudes were converted to PSF and auto-magnitudes using the median offset between PSF (or auto) magnitude and aperture magnitude for point sources from the whole Y1A1 data set. Our magnitude limit of $z_{\mathrm{PSF}} < 21.0$ is shown as the vertical line. Auto-magnitudes are intended to give the most precise estimate of total magnitudes for galaxies. We do not use auto-magnitudes in the analysis and they are included here for comparison with other work.

flat cosmology with $\Omega_{\mathrm{m0}} = 0.3$ and $H_0 = 70.0$ km s^{-1} Mpc^{-1} was used. The code used in this analysis makes use of the ASTROPY PYTHON package (Astropy Collaboration et al. 2013).

2 PHOTOMETRIC IMAGING DATA

2.1 Dark energy survey data

Here, we use the Year One First Annual (Y1A1) internal collaboration release of the DES data (Diehl et al. 2014; Drlica-Wagner et al., in preparation). These data cover ~ 1840 deg^2 of the Southern celestial hemisphere to a median 10σ point source (MAG_PSF) depth in AB magnitudes of 23.28, 23.6, 23.1, 22.3 and 20.8 in the *g, r, i, z* and *Y* bands, respectively. Catalogue source detection uses the SExtractor (Bertin & Arnouts 1996) image detection software in double image mode using the χ^2 detection image (Szalay, Connolly & Szokoly 1999) constructed from the combination of the *r, i* and *z* band images as the detection image.

The point source depths are calculated from area-weighted median aperture (MAG_APER_4) magnitude limits taken from the DES Mangle (Swanson et al. 2008) products at 10σ in a 2 arcsec diameter aperture values of 24.2, 23.9, 23.3, 22.5 and 21.2. See Fig. 1 for the *z*-band magnitude limit versus cumulative area. To convert these aperture depths to point source depths, the median differences between the 2 arcsec aperture magnitude and the point spread function (PSF) magnitude for point sources were used across the survey. The offsets (MAG_APER − MAG_PSF) are *g*: -0.4, *r*: -0.3, *i*: -0.2, *z*: -0.2, *Y*: -0.4 with the differences due to the differences in the average PSF widths induced by seeing for each waveband.

Once completed, DES will cover 5000 deg^2 in five optical bands with images taken using the DECam (Flaugher et al. 2015), which is mounted on the Blanco 4-m telescope at the Cerro Tololo Inter-American Observatory (CTIO). The data are then reduced using the DES data management process (Desai et al. 2012; Mohr et al. 2012). DECam is particularly suited to high-redshift survey work due to
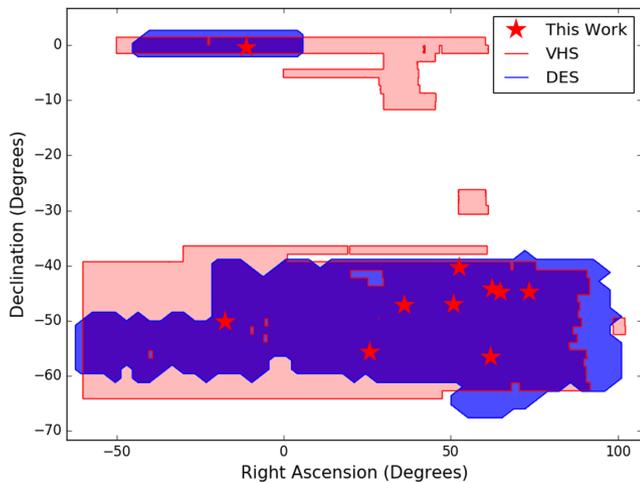
Figure 2. The sky coverage of the DES and VHS data used in this work. The blue area shows the DES footprint and the red area shows the VHS footprint. The overlap between the two surveys is shown in purple.

its large field of view (3 deg^2) and red sensitivity (∼50 per cent total transmission at 9000 Å). The data contained in the Y1A1 release were taken between 2013 August 15 and 2014 February 9. The Y1A1 release is shallower than the final survey depth and consists of 3707 co-added tiles covering two contiguous regions: one overlapping the Stripe 82 area imaged by the SDSS and one overlapping with the area covered by the South Pole Telescope (SPT). The tiles are co-add images made up of between one and five exposures in each of the five wavebands with an average coverage of 3.5 exposures making up each tile.

A magnitude limit of $z_{PSF} \leq 21.0$ was used in this work; this corresponds to an area of 1835 deg^2. Fig. 1 shows the cumulative area against depth for the data set in 2 arcsec diameter aperture, PSF and auto-magnitudes for stellar objects where we define stellar objects based on R15. Whilst auto-magnitudes are intended to give the most precise estimate of total magnitudes for galaxies, they can also be used for stellar objects. The SExtractor implementation of the routine is based on Kron (1980). We do not use auto-magnitudes in the analysis here; they are included here for comparison with other work noting the small offset for point sources between auto-magnitudes and PSF magnitudes, which may indicate a systematic overestimate in the auto-fluxes. The z-band limit used here is shown as the vertical line and is well above the 10σ limit. As we only used the area of DES covered by VHS as of 2014 February 1 (∼84 per cent), this reduced the total area available to 1533 deg^2. The overlap and location of these two surveys are shown in Fig. 2.

In this paper, DES magnitudes quoted are PSF magnitudes derived from PSF fluxes calculated using PSFs for each co-add tile measured as part of the DES reduction using PSFex (Bertin 2011). When other magnitude or flux measurements (e.g. aperture) are used, this is explicitly stated. All magnitudes are given in the AB system. Aperture magnitudes and fluxes from DES are given for a 2 arcsec diameter aperture with an aperture correction applied based on the PSF to compensate for missing flux outside the aperture unless otherwise stated. Corrected aperture fluxes were used in the model fitting calculations and the fluxes given in the paper are aperture-corrected fluxes unless otherwise stated. Aperture flux measurements were used, as they best represent the flux when the object was near or below the detection limit of the data.

2.2 VISTA Hemisphere Survey data

The VHS (McMahon et al. 2013) aims to carry out an NIR survey of ∼18 000 deg^2 of the Southern hemisphere to a depth 30 times fainter than the Two Micron All Sky Survey (2MASS) in two wavebands J and K_s. The survey uses the 4-m VISTA telescope (Sutherland et al. 2015) at ESO's Cerro Paranal Observatory in Chile. In the Southern Galactic Cap ∼5000 deg^2, which will overlap the DES area, is being imaged more deeply ($J_{AB} = 21.2$, $K_{s;\,AB} = 20.4$; 5σ point source depths) with partial coverage in H. This gives data in three bands (J, H and K_s) in the NIR at ∼1–2 µm. H-band data are not being taken over the full DES and some of the area used in this project does not have H-band imaging. The VHS data used in this work were taken between 2009 November 4 and 2014 February 1.

The VIRCAM camera (Dalton et al. 2006) used for VHS imaging has a sparse array of 16 individual 2k × 2k MCT detectors covering a region of 0.595 deg^2. In order to cover the full 1.5 deg^2 field of view of the camera six exposures are required. These exposures are then combined into one co-added tile as part of the pipeline processing. The data are processed with the VISTA Data Flow System at CASU (Emerson et al. 2004; Irwin et al. 2004; Lewis, Irwin & Bunclark 2010) and the science products are available from the ESO Science Archive Facility and the VISTA Science Archive (Hambly et al. 2004; Cross et al. 2012).

2.3 *Wide Infrared Survey Explorer* data

Longer wavelength data at 3.4, 4.6, 12 and 22 µm (known as *W1, W2, W3* and *W4*, respectively) were used from the all-sky *WISE* (Wright et al. 2010). The *WISE* satellite uses a 40-cm telescope with a camera containing four 1024×1024 arrays with a median pixel size of 2.757 arcsec and a field of view of 47×47 arcmin. The telescope scanned the sky and took multiple images giving co-add 5σ point source depths of $W1_{AB} = 19.3$, $W2_{AB} = 18.9$, $W3_{AB} = 16.5$ and $W4_{AB} = 14.6$. The co-add images have full width at half-maximum of 6.1 arcsec in the *W1, W2* and *W3* bands, and 6.4 arcsec in *W4*. Once the cryogenic fuel got exhausted in 2010 the telescope continued to survey the sky in the two shortest bands as part of the post-cryogenic *NEOWISE* mission phase. The two data sets were combined into the 2013 *WISE* AllWISE Data Release. The AllWISE co-add images are 4095 × 4095 pixels at 1.375 arcsec per pixel.

3 QUASAR CANDIDATE SELECTION

Following on from the selection method presented in R15 we have developed a selection method that uses all the photometric data (from *WISE*, VHS and DES) available for the objects. The selection method incorporated the first eight steps outlined in section 3 of R15 and is summarized in Table 1. Then the candidate list was matched to the VHS catalogue data to give J and K band magnitudes for the objects and was a fast way to remove artefacts such as cosmic rays that were present in only one of the surveys. Matching to VHS and keeping only objects with $Y_{AB} - J_{AB} < 1.0$ left 960 candidates from the original 4195 that satisfied the first stages of selection. The cuts used are shown in Figs 3 and 4. The $z - Y$ and $Y - J$ cuts were chosen to be the reddest cuts that excluded all known dwarf stars used in this analysis.

| Step	Description	Number removed	Number remaining
	Number of objects in data base		139,142,161
1	Steps 1–8b from R15[a]		
	$z_{PSF} \leq 21.0$ and $\sigma_z < 0.1$		
	$i_{PSF} - z_{PSF} < 1.694$		
	g_{PSF} and $r_{PSF} > 23.0$		
	σ_g and $\sigma_r > 0.1$		
	$z_{PSF} - Y_{PSF} < 0.5$		
	$Y_{PSF} < 23.0$	139,135,538	4195
2	$Y - J < 1.0$	3235	960
3	Remove chip edges in z band	498	462
4	Remove bad image areas	105	393
5	Remove objects bright in r	246	147

Note. [a]A magnitude limit of $z = 21$ was used rather than 21.5 in R15 and no point source separation.
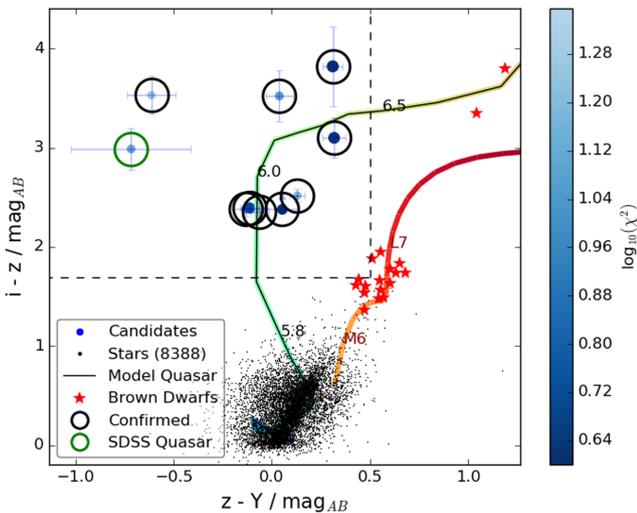
Figure 3. $z - Y$ versus $i - z$ colour–colour diagram shows the colour space used for the selection. The dashed lines show the $z - Y$ and $i - z$ colour cut limits used. This colour cut limit is the same as was used in R15 and was designed to help remove cool stars. The black points are stars taken from three tiles of DES data and the red stars are known brown dwarfs from Kirkpatrick et al. (2011) matched to the DES data. The red line shows the derived colour track for dwarf stars; the colour of the line corresponds to the colour of the line in Figs 5 and 6 as does the colour of the blue–green line that shows one of the quasar tracks used. The blue points give our candidate objects with higher ranked objects being darker in colour and larger in size. The black circled objects were followed up spectroscopically, and the green circle shows the known SDSS quasar. Objects with a good fit to the brown dwarf model are not shown on this plot. A large colour region around the predicted colour line is probed to account for the intrinsic variation in the SEDs of quasars as well as line-of-sight extinction in the sources and the uncertainties in the photometry for each object.

3.1 *WISE* list driven aperture photometry

As the *W1–W2* colour is a discriminant between quasars and cool stars, list-driven aperture photometry code was run on the unWISE images (Lang 2014). We use these unblurred co-adds from the *WISE* Atlas images. The unWISE co-add images are 2048 × 2048 pixels at the nominal native pixel scale, 2.75 per arcsec pixel, rather than the 4095 × 4095 images at 1.375 per pixel chosen in the AllWISE
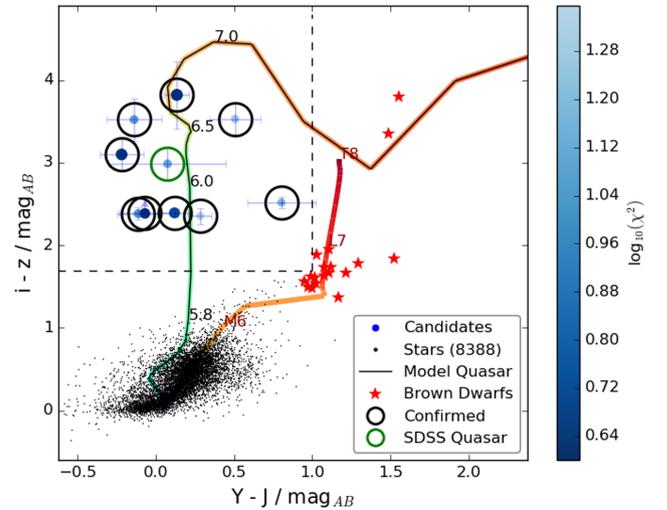
Figure 4. $Y - J$ versus $i - z$ colour–colour plot showing the reasoning behind the $Y - J$ colour cut. A colour limit of 1.0 (marked with a dashed line) removes all known cool dwarf stars whilst allowing us to probe as much parameter space as possible. In future work, we hope to loosen or remove this colour cut. The points in this figure follow the same schema as in Fig. 3. Objects with a good fit to the brown dwarf model are not shown in this plot.

Release. The blurred AllWISE images are better suited for source detection but the unblurred unWISE coadds used here have better resolution, and are therefore more appropriate for forced, list-driven photometry at known positions on the sky (Lang 2014). Forced photometry was done using IMCORE_LIST from version 1.0.26 of the CASUTOOLS software package (Irwin 1985).[3] The code was run for all objects in the VHS catalogue where the VHS sources were used as inputs as they are closer in wavelength than the DES sources and so were more likely to have a corresponding *WISE* source. The approach of using the *J*-band positions will also allow us to use these same catalogues as we push our search to higher redshift where we expect quasar candidates to no longer be detected in the shorter (*riz*) wavelength DES bands at all. An aperture radius of 2.5 pixels (~6.9 arcsec) was used for the list-driven photometry on the *WISE* images. This was chosen to match the aperture size used for the published *WISE* catalogues. Whilst a smaller aperture size would help to ensure that the flux came only from the specified object, it would also miss more of the *WISE* flux that is outside the aperture due to the PSF of *WISE*. A larger aperture can also include flux from neighbouring objects. An alternative approach would be to estimate the *WISE* fluxes using PSF-based weighting.

3.2 Photometric SED modelling, redshifts and stellar classification

To prioritize the candidates, a photometric redshift fit was carried out using a series of model spectral energy distributions (SEDs). Four quasar models (Maddox et al. 2012) based on the spectral templates in Maddox & Hewett (2006), with different levels of intrinsic reddening [$E(B - V) = 0.0, 0.025, 0.05, 0.10$ in the rest-frame quasar spectrum], were used in 0.1 redshift increments between 4.0 and 8.0 for the model fitting. The model is a parametric model where the continuum consists of two power laws (with slopes -0.42 and

[3] http://casu.ast.cam.ac.uk/surveys-projects/software-release

Table 2. Parameters from the fitting process for the confirmed quasars.

Name	Rank	$\chi^2_{\rm red}$ of best quasar model	Best $E(B-V)$	Best redshift	Spectroscopic redshift	$\chi^2_{\rm red}$ of best brown dwarf model	Best type	$\frac{\chi^2_Q}{\chi^2_{\rm BD}}$
VDES J0143−5545	9	3.15	0.100	6.1	6.25	38.87	M7	0.081
VDES J0224−4711	3	1.62	0.050	6.4	6.50	32.24	M7	0.050
VDES J0323−4701	10	3.35	0.000	6.1	6.25	15.02	M5	0.223
VDES J0330−4025	5	2.24	0.025	6.2	6.25	18.71	M7	0.120
VDES J0408−5632	8	3.10	0.000	6.0	6.03	13.76	M6	0.225
VDES J0410−4414	1	1.44	0.000	6.2	6.21	16.62	M6	0.087
VDES J0420−4453	6	2.54	0.000	6.0	6.07	19.44	M6	0.131
VDES J0454−4448[a]	2	1.55	0.000	6.0	6.10	18.81	M6	0.082
VDES J2250−5015	4	1.78	0.050	6.0	6.00	12.20	M8	0.146
VDES J2315−0023[b]	7	2.67	0.000	6.0	6.12	30.92	M5	0.086

Notes. [a]This object was found in R15.
[b]This object is SDSS J231546.57+002358.1 found in Jiang et al. (2008).

Table 3. Parameters from the fitting process for the 10 objects ranked highest to be low-mass cool stars or brown dwarfs. Only objects with photometry in all the available bands were included here.

Name	$\chi^2_{\rm red}$ of best quasar model	Best $E(B-V)$	Best redshift	$\chi^2_{\rm red}$ of Best brown dwarf model	Best type	$\frac{\chi^2_Q}{\chi^2_{\rm BD}}$
VDES J0419−5033	18.55	0.000	6.0	1.05	L0	17.67
VDES J0440−5258	11.48	0.000	6.0	1.43	L0	8.03
VDES J0516−5433	9.25	0.050	6.0	1.38	L3	4.53
VDES J0524−5710	19.37	0.000	5.9	0.82	M7	23.62
VDES J0541−5959	11.15	0.000	5.9	0.80	M7	13.94
VDES J2138−5853	18.69	0.000	5.9	1.36	M7	13.75
VDES J2248−4639	12.36	0.025	6.0	1.31	L1	9.44
VDES J2300−4432	13.88	0.000	6.0	1.06	M9	13.10
VDES J2307−0044	24.54	0.000	6.0	1.07	L0	22.93
VDES J2321−5655	6.66	0.000	5.2	1.10	M5	6.05

−0.17) that are joined at 2340 Å. Longward of 1 μm the flux is dominated by a single-temperature blackbody with $T = 1236$ K. On the top of this is an empirical quasar emission line spectrum. Shortward of the Ly α emission line the continuum flux is suppressed by a model of the Ly α forest absorption that is redshift dependent. All the flux shortward of the rest-frame Lyman-limit (912 Å) is removed. Thus, at all redshifts above $z = 5$, there should be zero flux in the DES g band that has <1 per cent of peak transmission at $\lambda > 5530$ Å. The flux from the model was integrated over all the DES and VHS wavebands as well as the *WISE W1* and *W2* bands. As the DES aperture fluxes do not include aperture corrections by default and SExtractor (Bertin & Arnouts 1996) does not return negative fluxes for PSF fluxes, aperture corrections were calculated to account for any flux that fell outside the aperture. It was necessary to have good measurements of the flux for very faint/undetected objects as all of our candidates are not present in the bluest DES bands. The aperture corrections were calculated using the median of the $\frac{\rm PSF_{flux}}{\rm Aperture_{flux}}$ for stellar objects. They were calculated for each individual DES image tile and applied separately for each tile. The objects were also compared to the derived brown dwarf colours from Skrzypek et al. (2015). As these colours were given in the UKIRT Infrared Deep Sky Survey (UKIDSS) Large Area Survey (LAS) and SDSS pass bands, colour terms (these are given in the Appendix) were calculated between the surveys using the overlap among DES, UKIDSS, VHS and SDSS in Stripe 82. The colours were then converted on to the AB system using the offsets given in Hewett et al. (2006). Table 2 shows the 10 objects followed up in this work, and Table 3 shows the 10 objects ranked most highly to

be brown dwarfs. Figs 5 and 6 show the results of the model fitting for the highest ranked quasar candidate and a probable low-mass star with spectral type M7.

The reduced χ^2 ($\chi^2_{\rm reduced}$) values were derived using the formula:

$$\chi^2_{i,\rm reduced} = \sum_{n=1}^{N} \left(\frac{{\rm data}_n - f_n({\rm model}_i)}{\sigma({\rm data})_n} \right)^2 \bigg/ (N-1), \qquad (1)$$

where for each model$_i$ we sum over $n = 1 \ldots N$ wavebands with $N - 1$ degrees of freedom.

When the photometric fitting method was first run, it was found that objects with unreliable non-Gaussian errors in their photometry, due for example to CCD chip edges and saturated objects, were contaminating the candidate list. These objects were then removed using image-based techniques. To remove objects with photometry affected by chip edges, the pixel values in a 30 arcsec box around the object were analysed and if more than a third had the same value the object was rejected; this also removes areas that have been masked with zeros in the image (such as saturated areas and bleed trails). It was found that a large number of the candidates appeared to have no measured flux in the g, r, or i bands, but there were also no other objects present with a region with radius of 30 arcsec around the location of the candidate in the image. It was found that these patches of image had very different noise properties compared to other parts of the image. To remove these, the median and the median absolute deviation (MAD) of the pixel values in a 30 arcsec box around the object were calculated. The MAD was used as it gives a robust estimate of the statistical dispersion of the data and is related to the standard deviation (σ) through $\sigma = 1.4826$ MAD. The pixel MAD
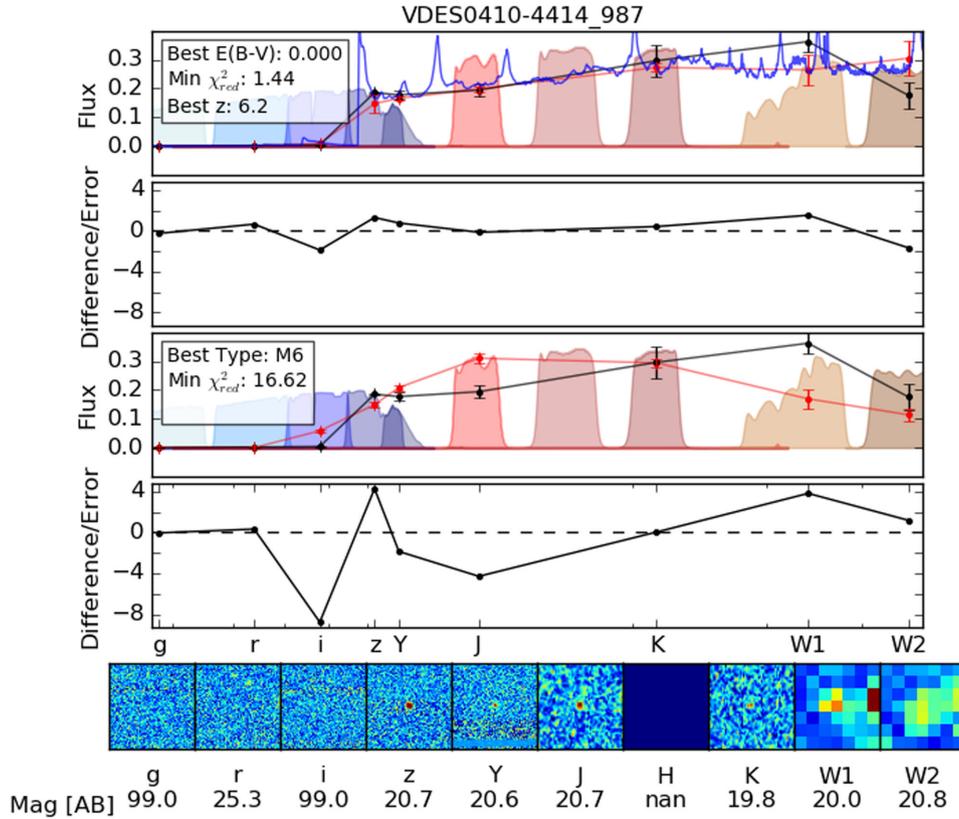
Figure 5. An example of the model fitting results for the highest ranked quasar in the sample. The top panel shows the best-fitting quasar model in red and the data with associated uncertainties in black. The filled areas show the filters for DES, VHS and *WISE*. The blue line shows the model quasar spectra used. The second panel down shows the residuals from the fit divided by the uncertainties on each point. The third and fourth panels show the same thing for the best-fitting cool star model. Along the bottom of the figure are 20 arcsec cutouts in each band with the AB magnitude in that band beneath.

was studied for a large number of images and the distribution of MAD values from 30 arcsec boxes across these images was found to be bimodal with a dip at ∼0.7. Objects with a MAD value less than this empirically derived threshold of 0.7 were removed. The bright *r*-band objects were removed as detailed in R15. These pixel level filtering steps are done after catalogue level selection as the image-based techniques are more computationally intensive than the catalogue ones, so it is more efficient to run them on the reduced candidate list rather than to create a completely clean list from the beginning. Furthermore, if the images are not available colocated to computational resources, network transfers can be prohibitive. Table 1 lists the number of candidates removed by each selection stage.

The photometric fitting was then run again on the 147 remaining candidates. Candidates were first ranked based only on their quasar reduced χ^2 values with the smallest reduced χ^2 sources having the highest ranking. Following this ranking, we visually inspected the candidates in ranked order to remove artefacts and junk sources, and also compared the quasar reduced χ^2 values to those obtained from a brown dwarf fit to the photometry. The likelihood of being a brown dwarf was calculated from the polynomial fits in Skrzypek et al. (2015). Objects where the reduced χ^2 to be a brown dwarf was comparable to or higher than that to be a quasar were removed.

We found that the reduced χ^2 values for the best-fitting quasar and low-mass star models often exceeded 3 and hence were ruled out at >99 per cent. At face value, this is indicative that neither model fitted the data. This could be interpreted to mean that the photometric measurements had systematic errors or the range of

SED models being considered was not representative of the underlying true distribution. We took a pragmatic approach and added a systematic photometric uncertainty to the statistical uncertainty in each waveband. Percentage errors in flux of 10 per cent, 10 per cent, 10 per cent, 20 per cent, 5 per cent, 5 per cent, 5 per cent, 5 per cent, 20 per cent and 20 per cent in *g, r, i, z, Y, J, H, Ks, W1* and *W2*, respectively, were added in quadrature to the statistical uncertainties as shown in equation (2)

$$\chi^2_{i,\text{reduced}} = \sum_{n=1}^{N} \left(\frac{\text{data}_n - f_n(\text{model}_i)}{\sigma(\text{data} + \text{model})_n} \right)^2 \bigg/ (N-1). \quad (2)$$

The resultant χ^2 values for the 10 highest ranked most probable quasars are shown in Table 2. The 10 objects with highest low-mass star SED probability are listed in Table 3 and have a range of best-fitting spectral types from *M5* to *L3*.

4 SPECTROSCOPIC OBSERVATIONS

Spectroscopic observations of the eight unconfirmed candidates were obtained between 2015 October and November using the European Southern Observatory's (ESO) 3.6-m New Technology Telescope (NTT) and the 8.1-m Gemini-South Telescope. The confirmed quasars from these spectroscopic follow-up runs are listed in Table 2. A summary of the observations, including the exposure times and grism/grating used, is given in Table 4 and a summary of the objects' properties is given in Table 5. Fig. 7 shows the spectra of the objects presented here along with the spectrum of
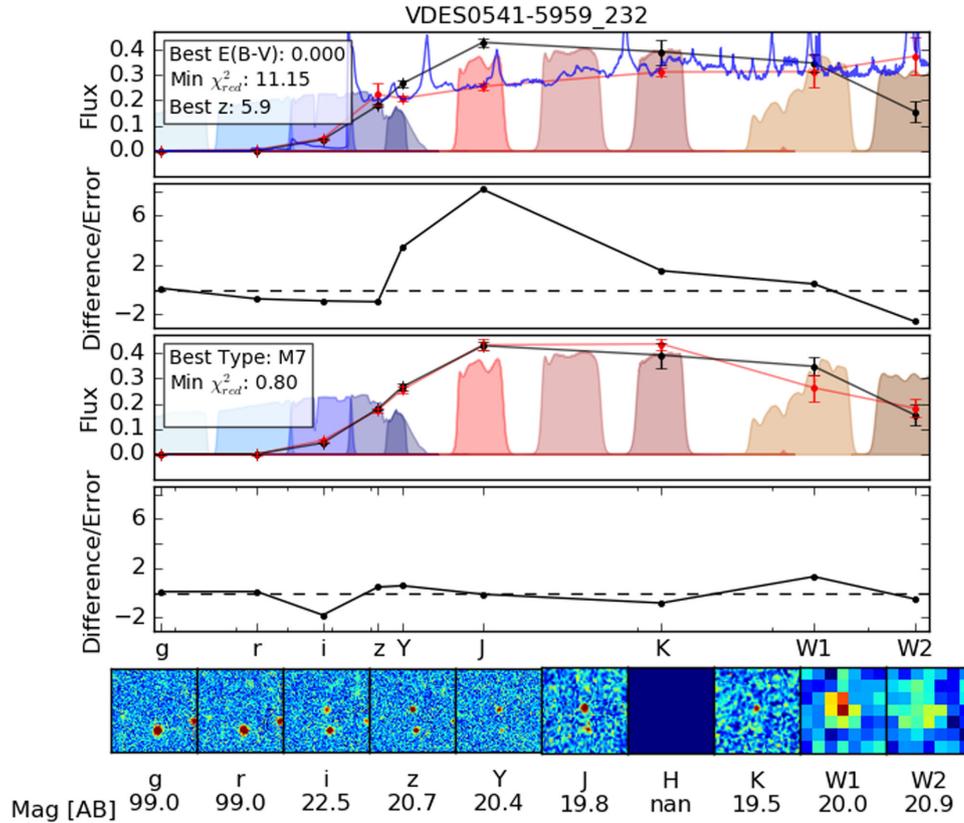
Figure 6. An example of the fitting results for the highest ranked low-mass cool star in the sample. The colours and lines are the same as in Fig. 5.

Table 4. Details of the spectroscopic observations.

Name	Telescope	Instrument	Exposure time (s)	Date	Filter	Grating/ Grism
VDES J0143−5545	NTT	EFOSC2	1200 + 1200 = 2400	09/11/2015	OG530	Gr#16
VDES J0224−4711	NTT	EFOSC2	1800 + 1800 = 3600	07/11/2015	OG530	Gr#16
VDES J0323−4701	GEMINI-SOUTH	GMOS-S	600 + 600 + 600 + 600 = 2400	22/11/2015	RG610_G0331	R400+_G5325
VDES J0330−4025	GEMINI-SOUTH	GMOS-S	600 + 600 + 600 + 600 = 2400	22/11/2015	RG610_G0331	R400+_G5325
VDES J0408−5632	NTT	EFOSC2	1200 + 1200 = 2400	08/11/2015	OG530	Gr#16
VDES J0410−4414	GEMINI-SOUTH	GMOS-S	600 + 600 + 600 + 600 = 2400	11/09/2015	RG610_G0331	R400+_G5325
VDES J0420−4453	GEMINI-SOUTH	GMOS-S	600 + 600 + 600 + 600 = 2400	04/09/2015	RG610_G0331	R400+_G5325
VDES J2250−5015	NTT	EFOSC2	1800 + 1800 = 3600	07/11/2015	OG530	Gr#16

the object detailed in R15, as it was rediscovered in this sample. Four of the objects were observed with the NTT at ESO's La Silla observatory over three nights from the 2015 October 7 to 9. The spectra were taken with the ESO Faint Object Spectrograph and Camera 2 (EFOSC2) (Buzzoni et al. 1984) and reduced using a custom set of PYTHON routines. Calibration data were taken during the afternoon preceding the observations or taken as part of the PESSTO project (Smartt et al. 2015). A 1.5-arcsec-width slit was used and the data were binned 2×2 on data readout. Due to the inclemency of the weather due to partial cloud coverage and the smaller mirror aperture the NTT data are of modest quality compared to the Gemini observations of the rest of the sample. Four of the objects were observed with the Gemini Multi-Object Spectrograph (GMOS; Hook et al. 2004) at the Gemini South Telescope as part of the 2015B queue observations using a 0.75 arcsec mask and reduced with a custom PYTHON reduction code. All the reduced spectra are shown in Fig. 7. A pipeline was written to reduce the two-dimensional spectra from both telescopes. The object was lo-

cated on the CCD and a Gaussian was fitted to a well-behaved area of the spectrum. Standard star observations were used to study the change of position of the spectrum in the spatial direction with wavelength. This was found to vary little with time and a general formula for the trace was derived. This could not be done from the quasar spectrum as it only covered a small wavelength range at the reddest end of the detector. To be sure that we were seeing no flux due to the intrinsic properties of the object rather than because we were extracting the wrong part of the two-dimensional spectrum this trace was positioned using the small area of spectrum we have. The derived Gaussian profile was then used to weight the spectrum extracted along the line of the trace. Once the spectrum had been extracted, the response function of the instrument was calculated using the standard star observations and the spectrum corrected. The different spectrum was then stacked together and the result was calibrated using the multiband photometry. Wavelength calibration was applied using arc lamp observations taken in the day prior to the observations.

Table 5. Properties of the quasars in this sample. Upper limits are given for the magnitude in a 2 arcsec diameter aperture. All magnitudes are given in AB.

Name	Ranking	DES tile name	RA (J2000)	Dec. (J2000)	g	r	i	z	Y	J	Ks	$W1$	$W2$
VDES J0143−5545	9	DES0145−5540	25.79265	−55.75297	>24.22	>23.83	24.03	20.50	21.11	20.61	20.09	19.39	19.00
			$01^h43^m10^s24$	$−55°45'10''68$			±0.19	±0.02	±0.12	±0.11	±0.18	±0.09	±0.10
VDES J0224−4711	3	DES0222−4706	36.11057	−47.19149	>23.47	>23.35	24.02	20.20	19.89	19.75	18.99	18.75	18.64
			$02^h24^m26^s54$	$−47°11'29''4$			±0.40	±0.02	±0.05	±0.06	±0.06	±0.05	±0.14
VDES J0323−4701	10	DES0325−4706	50.91808	−47.02226	>24.40	>24.10	24.30	20.78	20.74	20.88	20.51	20.31	20.51
			$03^h23^m40^s34$	$−47°01'20''13$			±0.26	±0.02	±0.07	±0.16	±0.26	±0.17	±0.30
VDES J0330−4025	5	DES0329−4040	52.61632	−40.42121	24.98	>23.80	23.76	20.66	20.34	20.56	19.99	19.55	19.58
			$03^h30^m27^s92$	$−40°25'16''4$	±0.37		±0.20	±0.02	±0.06	±0.13	±0.18	±0.09	±0.14
VDES J0408−5632	8	DES0407−5622	62.08012	−56.54134	>24.04	24.89	22.48	20.13	20.19	19.91	19.70	20.30	19.74
			$04^h08^m19^s23$	$−56°32'28''82$		±0.42	±0.10	±0.01	±0.05	±0.06	±0.14	±0.15	±0.13
VDES J0410−4414	1	DES0409−4414	62.51345	−44.24464	>24.01	25.31	>23.04	20.65	20.61	20.68	20.22	20.00	20.79
			$04^h10^m03^s23$	$−44°14'40''7$		±0.45		±0.02	±0.09	±0.13	±0.22	±0.12	±0.34
VDES J0420−4453	6	DES0421−4457	65.04727	−44.88993	>24.27	24.98	22.71	20.32	20.46	20.57	20.04	19.73	20.12
			$04^h20^m11^s34$	$−44°53'23''8$		±0.27	±0.07	±0.02	±0.06	±0.12	±0.19	±0.10	±0.21
VDES J0454−4448[a]	2	DES0453−4457	73.50744	−44.80864	>24.46	>24.09	22.64	20.24	20.36	20.24	20.11	19.62	19.70
			$04^h54^m01^s79$	$−44°48'31''1$			±0.05	±0.01	±0.05	±0.07	±0.18	±0.10	±0.15
VDES J2250−5015	4	DES2250−4957	342.50837	−50.26171	>23.60	>23.68	22.63	20.11	19.98	19.18	19.00	18.71	19.04
			$22^h50^m02^s01$	$−50°15'42''15$			±0.06	±0.01	±0.04	±0.21	±0.14	±0.06	±0.12
VDES J2315−0023[b]	7	DES2316−0041	348.94409	−0.39938	24.00	>23.62	23.81	20.83	21.54	21.47	–	20.65	–
			$23^h15^m46^s58$	$00°23'57''78$	±1.86		±0.20	±0.03	±0.30	±0.22		±0.31	

Notes. [a]This quasar was found in R15 and it is included here for completeness and to allow comparison between the different DES data releases and the different *WISE* reductions used.
[b]This is a known object (SDSS J231546.57−002358.1) discovered in Jiang et al. (2008).

4.1 Redshift determination

Redshifts were calculated by fitting a quasar model to the spectroscopic data. The section of the spectra blueward of Ly α was modelled using an exponential to account for the rapid decay to zero flux. A Gaussian centred at 1025.7 Å was used to approximate the Ly β emission feature seen in some of the spectra. Ly α emission was modelled using half a Gaussian which matched on to the exponential at 1215.67 Å. Redward of Ly α the N V, O I and Si IV+O IV lines were added using Gaussians centred at 1240.1, 1304.46 and 1397.8 Å, respectively (Tytler & Fan 1992). The section longward of 1215.67 Å then had a power law and a constant offset added to model the continuum emission.

This model was tested using the spectroscopic data from Fan et al. (2006). Whilst the spectroscopic data presented here do not cover the full range of lines input into the model, some of the test data covered the full range. This model was then fitted to the data using a χ^2 minimization to give the best estimate of the redshift. An example of the redshift fitting process is shown in Fig. 8.

The method was tested on the SDSS sample from Fan et al. (2006); there it was found to recover the redshifts presented with a median difference of −0.01 with $\sigma_{MAD} = 0.01$. The σ_{MAD} (median absolute deviation) is used as a robust estimator of the Gaussian standard deviation where $\sigma_{MAD} = 1.4826 \times MAD$. σ_{MAD} was used to give an estimate of the systematic uncertainty in the redshifts of 0.01 that is far larger than the statistical uncertainties from the fitting. As the data quality varies across the sample the uncertainties are going to be underestimated for the nosiest data. The calculated redshifts and the redshifts from Fan et al. (2006) were also compared with the redshifts presented in Carilli et al. (2010), as shown in Fig. 9. The median difference between our calculated redshifts and the redshifts from Carilli et al. (2010) was found to be 0.0 with $\sigma_{MAD} = 0.01$, whilst the median difference between the redshifts from Carilli et al. (2010) and Fan et al. (2006) was −0.02 with $\sigma_{MAD} = 0.01$.

## 5 QUASAR IONIZATION NEAR ZONES

The observed spectra of $z > 6$ quasars are characterized by intrinsic quasar continuum emission and emission lines longward of the Ly α emission line in the quasar rest frame. Shortward of Ly α in the quasar rest frame the most distinctive feature of the spectrum is the deficit of continuum emission due to H I Ly α and Lyman series absorption by the cosmologically distributed intervening Ly α forest. At $z > 6$, the optical depth from this neutral H I absorption is considerable and is often called the 'Gunn Peterson trough' where the neutral hydrogen fraction (f_{HI}) is $f_{Hi} > 10^{-3}$. Closer to the quasar the UV radiation from the quasar ionizes H I and the H I opacity is decreased. This highly ionized H II region in called a near zone and the size of this region is determined by the large-scale structure or clumpiness of the H I, the average neutral fraction, the UV luminosity of the quasar and the age of the expanding UV radiation front emitted by the quasar. Observations of the distribution of near zone sizes and the evolution with redshift of this distribution are important probes of the Universe in the epoch of reionization.

Near zone sizes were calculated using the method described in R15, which follows Fan et al. (2006) where the edge of the near zone is taken to be the point where the ratio of the observed spectra to the extrapolated continuum flux first falls below 0.1 blueward of the Ly α peak. The spectral resolution and signal-to-noise ratio of our four NTT spectra are too low to measure near zone sizes. Measured near zone size (R_{NZ}) measurements from the four Gemini spectra and from R15 are presented in Table 6. The near zone size of a quasar in a cosmologically expanding medium will depend on the intrinsic UV flux of the quasar below the Ly α transition at 1216 Å. Following Carilli et al. (2010), we normalize the measured near zone sizes (R_{NZ}) to a constant UV absolute magnitude $M_{1450} = -27$ with the equation given below:

$$R_{NZ,corrected} = R_{NZ} \times 10^{0.4(27.0+M_{1450})/3}.$$
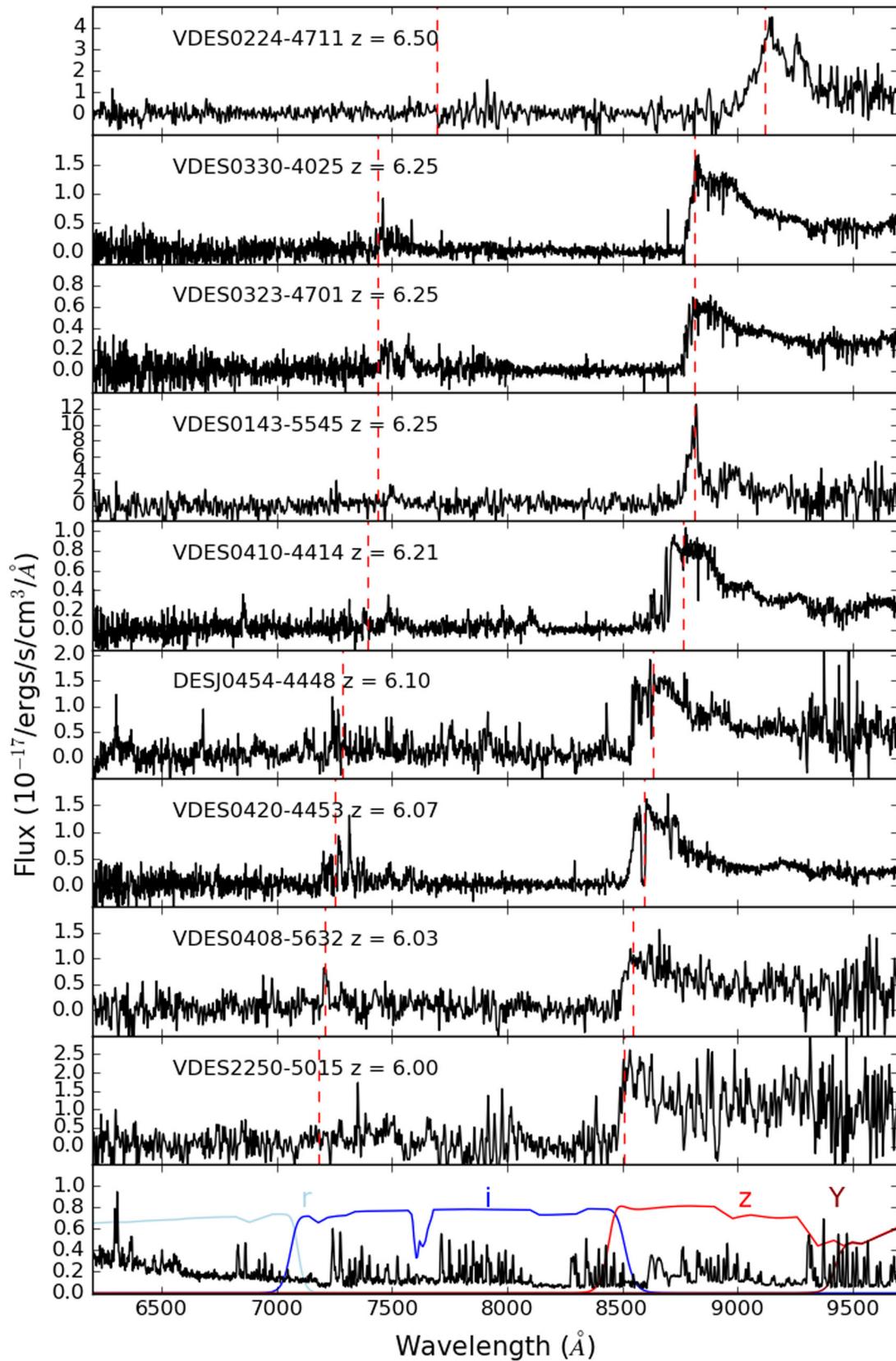
Figure 7. Reduced spectra of all the objects in this sample as well as the quasar discovered in R15 (DES J0454−4448), presented in redshift order. The vertical lines show the positions of Ly α and Ly β. The bottom plot gives an example error spectra taken from one of the quasars (VDES J0410−4414) and has the DES filters overplotted.
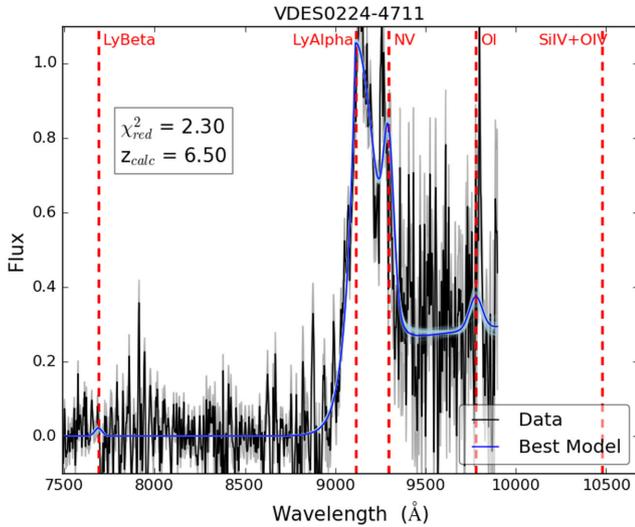
Figure 8. A model fit for the highest redshift quasar in this sample. The dashed lines show the centres of the lines used in the model. The data shown in black is the unsmoothed spectrum and the grey shaded area shows the uncertainty at each wavelength. The dark blue line is the best-fitting model and the light blue lines show 100 example model fits found during the fitting iterations. The reduced χ^2 from the fit and the calculated redshift are given in the inset panel.
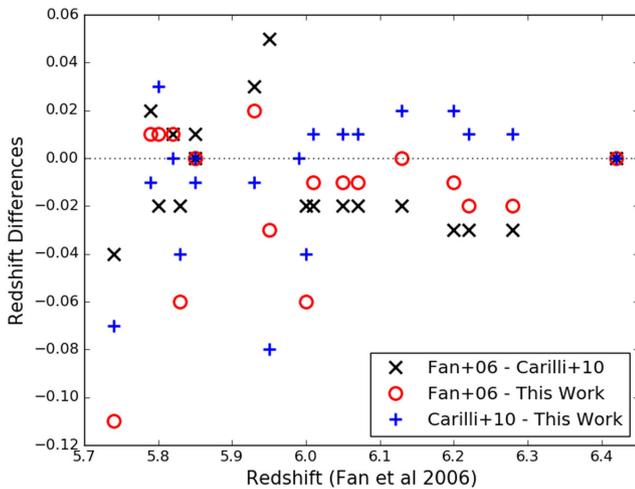
Figure 9. A comparison of the differences in redshifts between the fitting method used here and the results from Fan et al. (2006) and Carilli et al. (2010). The dashed line indicates the zero line.

Fig. 10 shows the distribution of corrected near zone size for 18 quasars with $6.0 < z < 6.5$ from Carilli et al. (2010) and four $z > 6.5$ quasars from Venemans et al. (2015b) and Mortlock et al. (2011) along with our new sample with $6.0 < z < 6.5$.

The blue solid line is the analytic solution from Keating et al. (2015) for the evolution of the normalized near zone sizes with redshift where the quasar has constant luminosity and the neutral fraction is not evolving with redshift. The decrease in size with increasing redshift is solely due to the increase in mean H I density as the Universe gets smaller in size at earlier redshifts. The dashed blue lines show the 15th and 85th percentiles about the median ($\sim \pm 1\sigma$) derived from simulations (Keating et al. 2015). The black dashed and black dot–dashed lines show linear fits by Carilli et al. (2010) and Venemans et al. (2015b), respectively.

The four new zones that we measure at $6.1 < z < 6.3$ span a large range from 3 to 9 Mpc. Two, VDES J0330−4025 and VDES J0323−4701, have relatively small corrected near zone sizes of ∼3 Mpc that could indicate that these two quasars are younger than the average quasar at this epoch and have relatively small lifetime ($10^6 - 10^7$ yr) and the ionized H II regions have not reached their maximum size due to the time taken for the ionizing radiation fronts to expand into the surrounding H I region. Alternatively if one ignores the effects of quasar lifetime to fully account for the small near zone sizes, the objects would need to be situated in regions of the Universe that are a factor of ∼10 above average H I density. Similar effects have been reported by Bolton et al. (2011) for the $z = 7.085$ quasar ULAS J1120+0641. The discovery of two $z \sim 6.2$ quasars with such small near zones indicates that care needs to be taken in interpreting small near zones as evidence for an increase in the neutral fraction. To further address this, more observational data are essential.

6 PROPERTIES OF INDIVIDUAL OBJECTS

Here, we give more details on some specific objects from our sample. A summary of the derived properties of the quasars presented here is given in Table 6. A comparison of these to known quasars is shown in Figs 11 and 12.

6.1 VDES J0143−5545 ($z = 6.23$)

VDES J0143−5545 was followed up with the NTT and found to have a very strong emission feature at ∼8820 Å, suggestive of a quasar with $z \sim 6.3$. This object was well fitted by the model with the highest level of reddening, $E(B - V) = 0.100$, at $z = 6.1$. This object has a very blue $z - Y$ of −0.61 due to the presence of the very strong Ly α emission line in the z filter. When the reddening fit was repeated without using the blended *WISE* data the object was best fitted by a model with $E(B - V) = 0.025$, suggesting that the *W1* and *W2* fluxes are affected by a nearby source.

6.2 VDES J0224−4711 ($z = 6.50$)

This candidate was ranked as the third most likely object to be a quasar in the candidate list with a very good fit to a reddened quasar model [$E(B - V) = 0.05$] at $z \sim 6.4$. It is quite bright with $z = 20.0$ and has a very red $i - z$ colour of 3.82. Follow-up of this object with the NTT showed a strong emission feature starting at ∼9100 Å giving a redshift of 6.50. The reddening fit was recalculated with the redshift fixed at the observed spectroscopic redshift of 6.50. At the spectroscopic redshift the photometry was best fitted by a reddened model with $E(B - V) = 0.05$. This object appears to have a very extended near zone but the modest quality of the spectral data means that this measurement has very large uncertainties. VDES J0224−4711 has $J_{AB} = 19.75$ and is the second most luminous quasar known with $z \geq 6.5$ and is 0.2 mag fainter than the most luminous quasar know with $z > 6.5$; PSO J0226+0302 with $z = 6.53$ and $J_{AB} = 19.51$ (Venemans et al. 2015b).

6.3 VDES J0323−4701 ($z = 6.25$)

VDES J0323−4701 was the lowest ranked candidate followed up. Spectroscopic observations with GMOS revealed a quasar at $z \sim 6.25$. This object was very red with $i - z = 3.52$ and was best fitted by a non-reddened quasar model with a slightly lower redshift of 6.10 than the spectroscopic one. The measured corrected near zone size
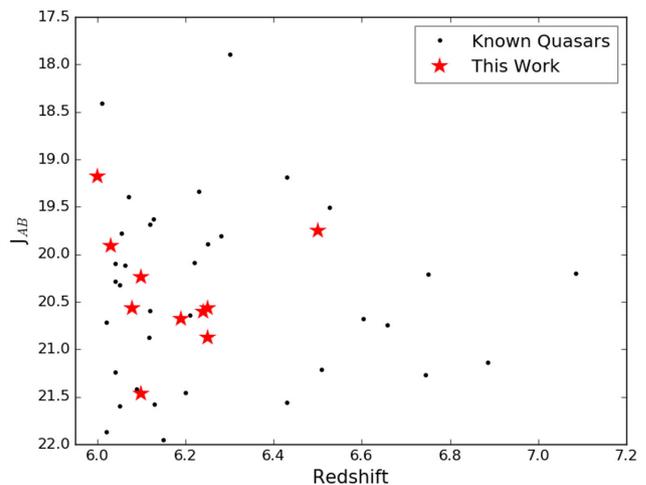
Table 6. Derived properties of the quasars in this sample. The near zone sizes for VDES J0454−4448 are taken from R15. Near zone sizes are not given for all objects as the data quality was not good enough.

Name	Redshift	M_{1450}	R_{NZ}	$R_{NZ, corrected}$
VDES J0143−5545	6.25 ± 0.01	-25.65 ± 0.12	–	–
VDES J0224−4711	6.50 ± 0.01	-26.93 ± 0.05	–	–
VDES J0323−4701	6.25 ± 0.01	-26.02 ± 0.07	$2.1 ^{+0.6}_{-0.5}$ Mpc	$2.8 ^{+0.8}_{-0.7}$ Mpc
VDES J0330−4025	6.25 ± 0.01	-26.42 ± 0.06	$2.1 ^{+0.6}_{-0.5}$ Mpc	$2.5 ^{+0.7}_{-0.6}$ Mpc
VDES J0408−5632	6.03 ± 0.01	-26.51 ± 0.05	–	–
VDES J0410−4414	6.21 ± 0.01	-26.14 ± 0.09	$6.9 ^{+0.5}_{-0.5}$ Mpc	$9.0 ^{+0.6}_{-0.7}$ Mpc
VDES J0420−4453	6.07 ± 0.01	-26.25 ± 0.06	$4.3 ^{+0.6}_{-1.0}$ Mpc	$5.3 ^{+0.8}_{-1.2}$ Mpc
VDES J0454−4448[a]	6.10 ± 0.01	-26.36 ± 0.05	$4.1 ^{+1.1}_{-1.2}$ Mpc	$4.8 ^{+1.3}_{-1.4}$ Mpc
VDES J2250−5015	6.00 ± 0.01	-26.80 ± 0.04	–	–

Note. [a]This object was found in R15.
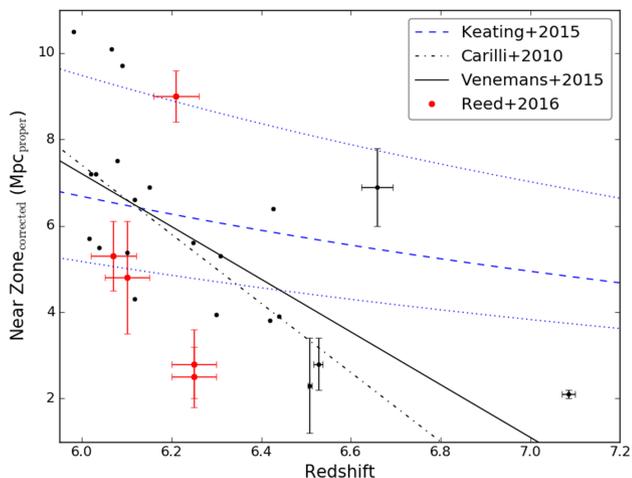
Figure 10. A comparison of the theoretical predictions and observations for high-redshift quasar near zone sizes. The black line shows the fit to the observational data from Carilli et al. (2010) and the black dot–dashed line is the fit from Venemans et al. (2015b). The blue line shows the theoretical fit from Keating et al. (2015) and the blue dotted lines are the 25th and 75th percentile for the range of near zone sizes that they found. The black points show near zone sizes from known quasars in the literature. The red points are some of the quasars in this sample. Objects with poor signal-to-noise spectra were not included here.

Figure 11. Here, the absolute magnitude calculated at 1450 Å in the rest frame is shown against redshift. The M_{1450} was estimated from the *Y*-band magnitude of the objects.

Figure 12. The apparent AB magnitude of these quasars in the *J*-band is shown against their redshifts compared with known quasars.

of 2.8 proper Mpc could indicate above average IGM density or a young age for this quasar.

6.4 VDES J0330−4025 ($z = 6.25$)

VDES J0330−4025 lies within $10°$ on the sky of the other quasar with a small near zone. VDES J0323−4701 also has a redshift of 6.25, so they could lie in a correlated region of the Universe with above-average IGM overdensity. The size of this region would be of Gpc scale and therefore unlikely to be in the standard cosmology.

6.5 VDES J0454−4448 ($z = 6.10$)

VDES J0454−4448 was the first $z \sim 6$ quasar identified from DES and was the subject of R15; details of the spectroscopic observations are included therein. It is included here as it was covered again by the year one release from the DES and was the second highest ranked candidate in the independent data analysis in this paper. The redshift was recalculated for this object as part of this analysis and was found to be 6.10 ± 0.01, which is consistent with the value given in R15 of 6.09 ± 0.03.

6.6 VDES J2250−5015 (z = 6.00)

This object was ranked fourth by the selection code with a good fit to a model with $E(B − V) = 0.05$ and a predicted redshift of 6.0. Follow-up spectroscopy with the NTT gives a redshift of 6.00. This source was the brightest in our sample with $z = 20.11$. VDES J2250−5015 has a fairly red $i − z$ colour of 2.52 and has a very red $Y − J$ colour of 0.80. The reddening fit was repeated with the redshift fixed at the calculated one and without using the *WISE* data as the close proximity of another source might be influencing this. This resulted in a model with more reddening [$E(B − V) = 0.1$] being chosen as the best fit. The red $Y − J$ colour of this object could be due to the reddening.

6.7 VDES J2315−0023 (z = 6.12)

The seventh most likely ranked candidate was a known quasar (SDSS J231546.57−002358.1) from the SDSS survey for quasars in stripe 82 (Jiang et al. 2008). Their spectroscopic follow-up found it to have $z = 6.117$ that is slightly higher than our photometric estimate of 6.0.

7 ANALYSIS OF SELECTION METHOD

There are seven previously known quasars with $z ≥ 5.80$ in the area covered by the data used in this study. Two are recovered by the selection criterion, VDES 0454−4448 ($z = 6.10$) from R15 and SDSS J2315+0023 from Jiang et al. (2008), as discussed in Section 6. The $z = 5.8$ quasar, SDSS J000552.34000655.8, discovered in Fan et al. (2004) is bluer than our $i_{DES} − z_{DES}$ selection and is not selected. This colour is indicative of being at a lower redshift than this selection method probes. The three quasars in Jiang et al. (2009) and the radio selected $z = 5.95$ quasar (SDSS J222843.54+011032.2) (Zeimann et al. 2011) that overlap the area have $z_{DES} > 21.0$ and therefore are fainter than our selection limit.

The automatic ranking of candidates in the candidate list allows visual inspection to be prioritized. This will be particularly useful once the full DES area is available for study, as there will be a large number (∼500) of candidate objects. This also means that looser colour cuts can be used to narrow down the data slightly allowing more unusual objects to be discovered. One such object is VDES J2250−5015 whose red colour in $Y − J$ would have caused it to be rejected by previous searches (Venemans et al. 2015a; Bañados et al. 2016). The Y- and J-band photometry of VDES J2250−5015 is reliable and suggests that the very red colour is real and due to intrinsic properties of the object.

The SED model fitting selection method presented here also allows the expansion of the candidate list without increasing the need for visual inspection as objects can be double checked in the ranked order. This is because most of the types of junk (cosmic rays, bleed trails, saturation issues, etc.) that contaminate the list are classified as very unlikely to be quasars. The astrophysical contaminants of the list (primarily cool stars) are also down weighted through this method. Our future aim is to be able to run the selection criteria over the entire input list without any need for colour cuts and using the reduced $χ^2$ fits as discriminators. At the moment, the colour selection is required to narrow down the list enough to make the image-based steps run more rapidly. Improvements in the analysis code will allow this to be done for a larger number of images more rapidly. The catalogue-based steps and the fitting steps are both fast enough (10^8 sources from ∼1500 deg² sources in less than 24 h on a single 4 GHz core) that they will be easily expanded to the larger ∼5000 deg² DES data set when it is released.
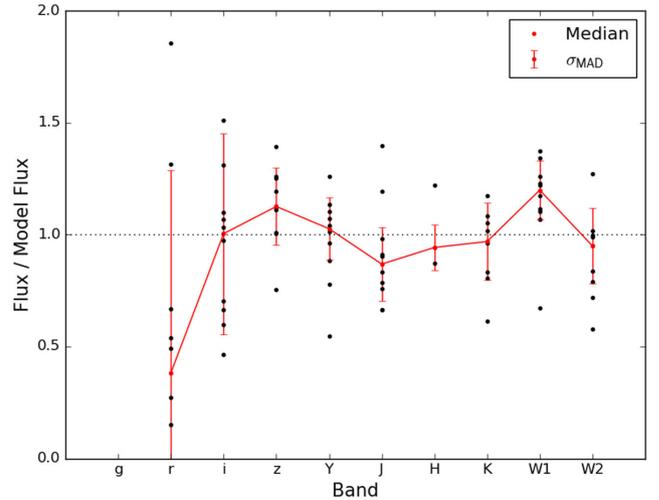

Figure 13. The black points are the measured flux values for the sample of 10 quasars divided by the flux derived from the best-fitting model. The red points are the medians of the ratio values in each band. The red error bars show the $1σ$ uncertainty derived from the MAD. No g band is shown as the model flux was mostly zero.

In this version of the selection code, objects with a high probability of being a brown dwarf are not rejected automatically but removed on an object-by-object basis when image cutouts of the object are checked. An improvement to the method would be to have automatic removal of these objects, as this will be more important for larger candidate lists generated either by relaxing the colour cuts or by a larger input data set. The confirmed quasars compared to the rest of the sample are shown in terms of reduced $χ^2$ to be either a star or a quasar in Fig. 15. It can be seen that the selected objects are well separated from the rest of the sample. Due to the inclement weather we did not have time to follow-up any objects further down the ranking and so do not know if the dashed lines should be relaxed to select a complete sample. The candidates in the bottom right region are junk (such as cosmic rays and objects affected by saturation) as confirmed by visual inspection.

In Section 3.2, our implemented SED fitting included an arbitrary systematic flux uncertainty. Now we have a spectroscopically confirmed sample and we analyse the residuals from the best-fitting models. In Fig. 13, we show the ratio of the observed flux to the best-fitting model flux for each quasar, the sample median and the $σ_{MAD}$. These show that the best-fitting models agree within the uncertainties.

The scatter in the ratios as described by the $σ_{MAD}$ is shown in Fig. 13. The values for these ratios in the bands that are unaffected by the Ly $α$ forest are similar to the values assumed in the fitting as described in Section 3.2. In r and i, the large scatter is from stochastic scatter in Ly $α$ forest and photometric statistical errors. In a future paper with a larger sample of confirmed quasars, we will investigate the scatter in terms of the model. There is some evidence for excess flux in the *W1* band that is probably due to the large aperture used resulting in flux from neighbouring objects. Since quasars are redder in *W1–W2* than the foreground galaxy and stellar populations, the *W2* band is less affected.

Fig. 14 shows the absolute continuum magnitude at a rest-frame wavelength of 1450 Å calculated from each of the four model quasar spectra used in this work. For this calculation, the models were scaled to have an observed integrated z-band magnitude of 21.0. This figure shows how the effect of the IGM absorption shortward of Ly $α$ reduces the flux in the z waveband. As a result a brighter
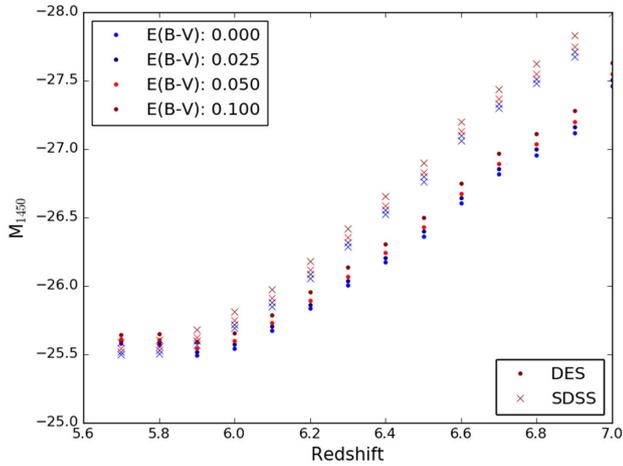
Figure 14. The absolute magnitude at 1450 Å for our four quasar models shown over a range of redshifts. The models were scaled to have a z-band magnitude of 21.0.
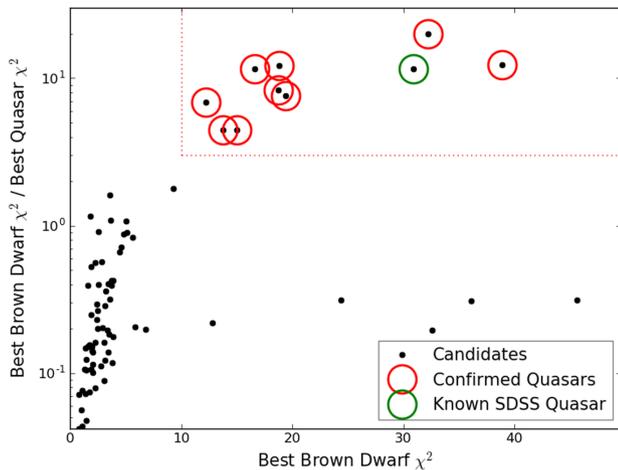
Figure 15. The known quasars were used to derive cuts to automatically select quasar candidates. These cuts are shown as the red dotted lines. The points circled in black are DES quasars and the object circled in green is a known SDSS quasar. It can be seen that these cuts separate the known quasars well from the rest of the sample. Due to inclement weather the object between the locus of points and the delimited box has not been followed up.

intrinsic M_{1450} is required for detection at a magnitude limit of 21. The selection criteria presented here are not designed to select objects above $z \sim 6.5$ due to the $z - Y$ colour limit shown in Fig. 3.

The code is written to allow different models to be easily inserted and tested, meaning that as additional models become available we can also compare to these. This will allow us to search for a wider variety of quasar types. For example, we hope to include models with a wider range of extinctions and at a finer sampling in extinction and redshift. Different treatments of the Ly α forest and different properties of the IGM can also be incorporated.

8 SUMMARY AND CONCLUSIONS

We have presented the photometric selection, statistical classification and spectroscopic confirmation of eight new high-redshift $6.0 < z < 6.5$ quasars with $z_{AB} < 21.0$, selected without any morphological star–galaxy classification from $\sim$1500 deg^2 using SED model fitting to photometric data from the DES (g, r, i, z, Y), the VHS (J, H, K) and the *WISE* (*W1*, *W2*). Starting from

over 100 million photometric sources, we used objective and repeatable machine-based techniques to select 147 quasar candidates. Probable cool stars were then removed based on their photometric classification and the candidates ranked before they were observed. Candidates were then visually inspected in their ranked order and those that passed observed. Our spectral confirmation success rate is 100 per cent without the need for follow-up photometric observations as used in other studies of this type. Combined with automatic removal of the main types of non-astrophysical contaminants, the method allows large data sets to be processed without human intervention and without being overrun by spurious false candidates. Of the highest redshift quasars VDES J0224−4711 (that has $J_{AB} = 19.75$) is the second most luminous quasar known with $z \geq 6.5$ and is 0.2 mag fainter than the most luminous quasar know with $z > 6.5$; PSO J0226+0302 with $z = 6.53$ and $J_{AB} = 19.51$ (Venemans et al. 2015b).

Candidates were ranked based on the ratio of reduced χ^2-statistic values for the best-fitting quasar model compared to the best-fitting stellar model. This approach is extendable to other photometric systems and imaging surveys (e.g. LSST and Euclid), in contrast to colour cut based criteria widely used in other high-redshift quasar searches.

A new quasar redshift determination algorithm has been developed based on the onset of the Ly α forest and a fit to the Ly α emission line using a semi-Gaussian and an exponential. The technique is validated on a sample of quasar that also has CO and Mg II emission line redshifts from Carilli et al. (2010) and find that our empirical fitting technique has a median difference of 0.003 and the distribution has $\sigma_{MAD} = 0.01$.

We have measured the sizes of the quasar ionization near zones for four of the new quasars and the $z = 6.00$ quasar J0454−4448 from R15 as shown in Fig. 10. The four new zones that we measure at $6.1 < z < 6.3$ span a large range from 3 to 9 Mpc. Two, VDES J0330−4025 and VDES J0323−4701, have relatively small corrected near zone sizes of $\sim$3 Mpc that could indicate that these two quasars are younger than the average quasar at this epoch and have relatively small lifetime ($10^6 - 10^7$ yr) and the ionized H II regions have not reached their maximum zone size due to the time taken for the ionizing radiation fronts to expand into the surrounding H I region. Alternatively, if one ignores the effects of quasar lifetime to fully account for the small near zone sizes the objects would need to be situated in regions of the Universe that are a factor of $\sim$10 above average H I density. Similar effects have been reported by Bolton et al. (2011) for the $z = 7.085$ quasar ULAS J1120+0641. The discovery of two $z \sim 6.2$ quasars with such small near zones indicates that care needs to be taken in interpreting small near zones as evidence for an increase in the neutral fraction. To further address this more observational data is essential.

We also present a robust parametric redshift estimating technique based on the onset of the Ly α forest that gives comparable accuracy Mg II and CO-based redshift estimators.

REFERENCES

Astropy Collaboration et al., 2013, A&A, 558, A33
Bañados E. et al., 2016, ApJS, 227, 11
Banerji M. et al., 2015, MNRAS, 446, 2523
Becker G. D., Rauch M., Sargent W. L. W., 2007, ApJ, 662, 72
Bertin E., 2011, in Evans I. N., Accomazzi A., Mink D. J., Rots A. H., eds, ASP Conf. Ser. Vol. 442, Astronomical Data Analysis Software and Systems XX. Astron. Soc. Pac., San Francisco, p. 435
Bertin E., Arnouts S., 1996, A&AS, 117, 393
Bolton J. S., Haehnelt M. G., 2007, MNRAS, 374, 493
Bolton J. S., Haehnelt M. G., Warren S. J., Hewett P. H., Mortlock D. J., Venemans B. P., McMahon R. G., Simpson C., 2011, MNRAS, 416, L70
Buzzoni B. et al., 1984, The Messenger, 38, 9
Carilli C. L. et al., 2010, ApJ, 714, 834
Carnall A. C. et al., 2015, MNRAS, 451, L16
Cross N. J. G. et al., 2012, A&A, 548, A119
Dalton G. B. et al., 2006, in McLean I. S., Iye M., eds, Proc. SPIE Conf. Ser. Vol. 6269, The VISTA Infrared Camera. SPIE, Bellingham, p. 62690X
Desai S. et al., 2012, ApJ, 757, 83
Diehl H. T. et al., 2014, in Alison B. P., Chris R. B., Robert L. S., eds, Proc. SPIE Conf. Ser. Vol. 9149, Observatory Operations: Strategies, Processes, and Systems V. SPIE, Bellingham, p. 91490V
Emerson J. P. et al., 2004, in Quinn P. J., Bridger A., eds, Proc. SPIE Conf. Ser. Vol. 5493, Optimizing Scientific Return for Astronomy through Information Technologies. SPIE, Bellingham, p. 401
Fan X., Hennawi J. F., Richards G. T., Strauss M. A., 2004, AJ, 128, 515
Fan X. et al., 2006, ApJ, 132, 117
Flaugher B. et al., 2015, AJ, 150, 150
Gunn J. E., Peterson B. A., 1965, ApJ, 142, 1633
Hambly N. C., Mann R. G., Bond I., Sutorius E., Read M., Williams P., Lawrence A., Emerson J. P., 2004, in Quinn P. J., Bridger A., eds, Proc. SPIE Conf. Ser. Vol. 5493, Optimizing Scientific Return for Astronomy through Information Technologies. SPIE, Bellingham, p. 423
Hewett P. C., Warren S. J., Leggett S. K., Hodgkin S. T., 2006, MNRAS, 367, 454
Hook I. M., Jørgensen I., Allington-Smith J. R., Davies R. L., Metcalfee N., Murowinski R. G., Crampton D., 2004, PASP, 116, 425
Irwin M. J., 1985, MNRAS, 214, 575
Irwin M. J. et al., 2004, in Quinn P. J., Bridger A., eds, Proc. SPIE Conf. Vol. 5493, Optimizing Scientific Return for Astronomy through Information Technologies. SPIE, Bellingham, p. 411
Jarrett T. H. et al., 2011, ApJ, 735, 112
Jiang L., Fan X., Annis J., Becker R. H., White R. L., Chiu K., Lin H., Lupton R. H., 2008, AJ, 135, 1057
Jiang L. et al., 2009, AJ, 138, 305
Jiang L. et al., 2016, ApJ, 833, 222
Keating L. C., Haehnelt M. G., Cantalupo S., Puchwein E., 2015, MNRAS, 454, 681
Kirkpatrick J. D., Cushing M. C., Gelino C. R., Griffith R. L., Skyrutskie M. F., Marsh K. A., Wright E. L., Mainzer A., 2011, ApJS, 197, 19
Kron R. G., 1980, ApJS, 43, 305
Lang D., 2014, AJ, 147, 108
Lewis J. R., Irwin M., Bunclark P., 2010, in Mizumoto Y., Morita K.-I., Ohishi M., eds, ASP Conf. Ser. Vol. 434, Astronomical Data Analysis Software and Systems XIX. Astron. Soc. Pac., San Francisco, p. 91
McMahon R. G., Banerji M., Gonzalez E., Koposov S. E., Bejar B. V. J., Lodieu N., Rebolo R. VHS Collaboration, 2013, The Messenger, 154, 35
Maddox N., Hewett P. C., 2006, MNRAS, 367, 717
Maddox N., Hewett P. C., Péroux C., Nestor D. B., Wisotzki L., 2012, MNRAS, 424, 2876
Mohr J. J. et al., 2012, in Radziwill N. M., Chiozzi G., eds, Proc. SPIE Conf. Ser. Vol. 8451, The Dark Energy Survey Data Processing and Calibration System. SPIE, Bellingham, p. 84510D
Mortlock D. J. et al., 2011, Nature, 474, 616
Mortlock D. J., Patel M., Warren S. J., Hewett P. C., Venemans B. P., McMahon R. G., Simpson C., 2012, MNRAS, 419, 390
Planck Collaboration XIII, 2015, A&A, 594, A13
Reed S. L., McMahon R. G., Banerji M., Becker G. D., Gonzalez-Solares E., Martini P., Ostrovski F., Rauch M., 2015, MNRAS, 454, 3952 (R15)
Skrzypek N., Warren S. J., Faherty J. K., Mortlock D. J., Burgasser A. J., Hewett P. C., 2015, A&A, 574, A78
Smartt S. J., Valenti S., Fraser M., Inserra C., Young D. Y., Sullivan M., Pastorello A., Benetti S., 2015, A&A, 579, A40
Sutherland W., Emerson J., Dalton G., Atad-Ettedgui E., Beard S., Bennett R., Bezawada N., Born A., 2015, A&A, 575, A25
Swanson M. E. C., Tegmark M., Hamilton A. J. S., Hill J. C., 2008, MNRAS, 387, 1391
Szalay A. S., Connolly A. J., Szokoly G. P., 1999, AJ, 117, 68
The Dark Energy Survey Collaboration, 2005, preprint (astro-ph/0510346)
Tytler D., Fan X.-M., 1992, ApJS, 79, 1
van Dokkum P. G., 2001, PASP, 113, 1420
Venemans B. P. et al., 2013, ApJ, 779, 24
Venemans B. P. et al., 2015a, MNRAS, 453, 2259
Venemans B. P. et al., 2015b, ApJ, 801, L11
Willott C. J. et al., 2010, AJ, 139, 906
Wright E. L. et al., 2010, ApJ, 140, 1868
Zeimann G. R., White R. L., Becker R. H., Hodge J. A., Stanford S. A., Richards G. T., 2011, ApJ, 736, 57

APPENDIX: COLOUR TERMS

The colour terms used in this analysis are included here for completeness:

$$H_{VHS} - H_{UKIDSS} = -0.01(i - z)_{SDSS} + 0.02$$
$$i_{DES} - i_{SDSS} = -0.30(i - z)_{SDSS} + 0.02$$
$$J_{VHS} - J_{UKIDSS} = -0.01(i - z)_{SDSS} - 0.02$$

$$K_{VHS} - K_{UKIDSS} = 0.04(i - z)_{SDSS} - 0.07$$
$$Y_{DES} - Y_{UKIDSS} = 0.09(i - z)_{SDSS} - 0.08$$
$$z_{DES} - z_{SDSS} = -0.07(i - z)_{SDSS} - 0.01.$$

Figs A1 and A2 show the fits for the full range of models used in this work for the highest ranked quasar and the highest ranked brown dwarf.
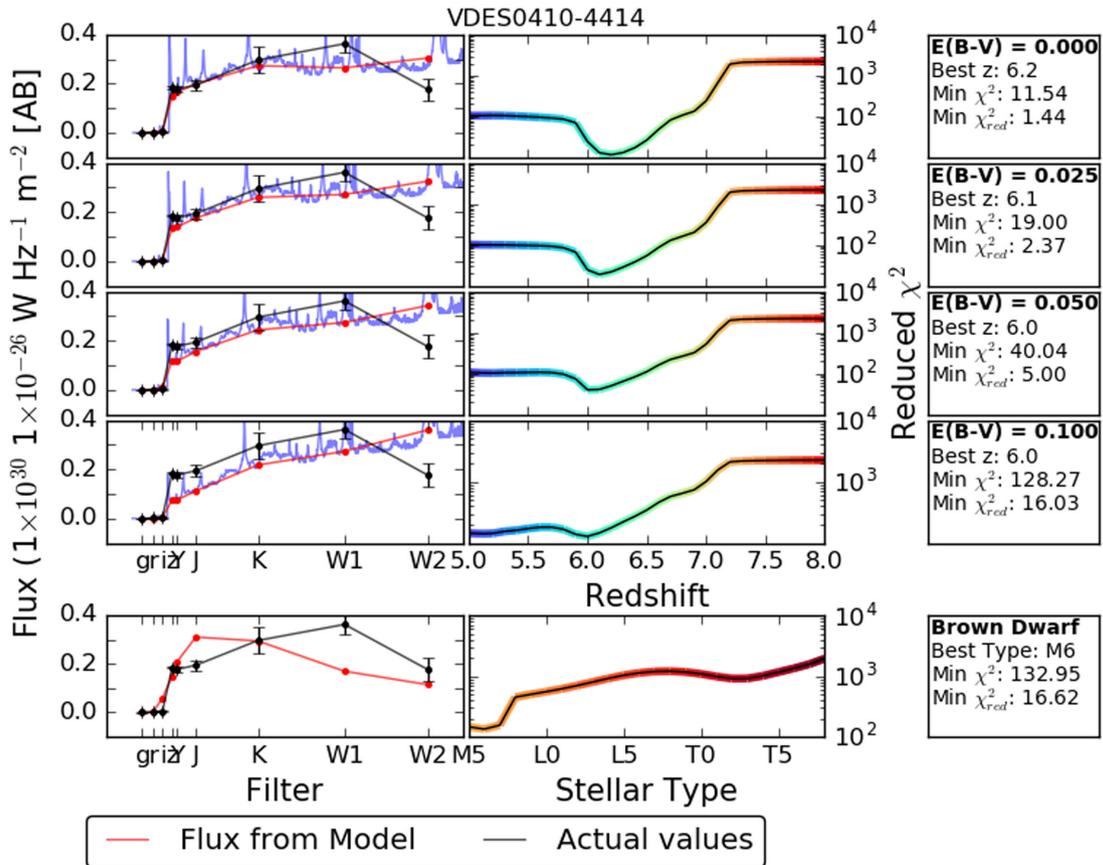
Figure A1. An example of the fitting results for the highest ranked quasar in the sample. The four different reddening models and the brown dwarf fit are shown in the left column of plots and the right column shows the reduced χ^2 fits for the range of redshifts/models considered. The brown dwarf model is clearly different from any of the quasar models. Note the different scales on the χ^2 plots.
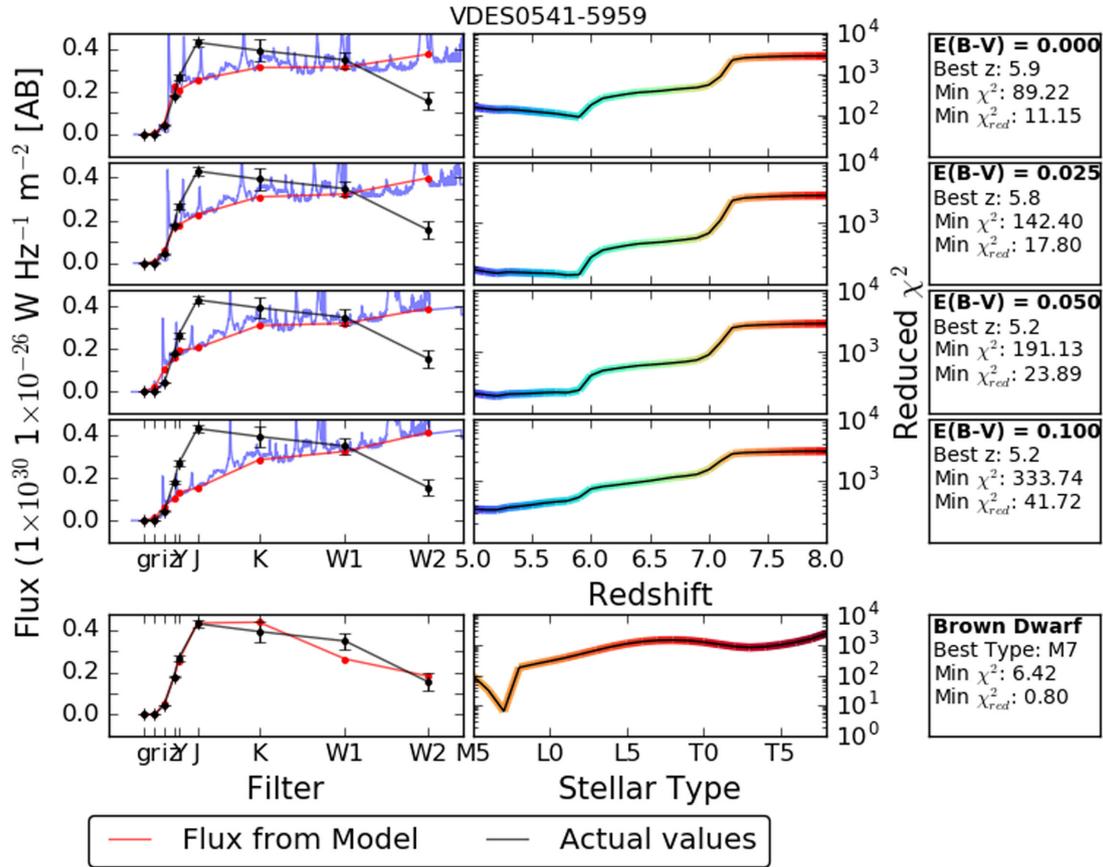
Figure A2. An example of the fitting results for a probably brown dwarf found in the sample. The four different reddening models and the brown dwarf fit are shown in the left column of plots and the right column shows the reduced χ^2 fits for the range of redshifts/models considered. It can be seen that the brown dwarf model is closer to the data than any of the quasar models. Note the different scales on the χ^2 plots.

[1]*Institute of Astronomy, University of Cambridge, Madingley Road, Cambridge CB3 0HA, UK*

[2]*Kavli Institute for Cosmology, University of Cambridge, Madingley Road, Cambridge CB3 0HA, UK*

[3]*Center for Cosmology and Astro-Particle Physics, The Ohio State University, Columbus, OH 43210, USA*

[4]*Department of Astronomy, The Ohio State University, Columbus, OH 43210, USA*

[5]*Department of Physics & Astronomy, University College London, Gower Street, London WC1E 6BT, UK*

[6]*Department of Physics and Electronics, Rhodes University, PO Box 94, Grahamstown 6140, South Africa*

[7]*Fermi National Accelerator Laboratory, PO Box 500, Batavia, IL 60510, USA*

[8]*CNRS, UMR 7095, Institut d'Astrophysique de Paris, F-75014, Paris, France*

[9]*Sorbonne Universités, UPMC Univ Paris 06, UMR 7095, Institut d'Astrophysique de Paris, F-75014, Paris, France*

[10]*Kavli Institute for Particle Astrophysics & Cosmology, PO Box 2450, Stanford University, Stanford, CA 94305, USA*

[11]*SLAC National Accelerator Laboratory, Menlo Park, CA 94025, USA*

[12]*Laboratório Interinstitucional de e-Astronomia - LIneA, Rua Gal. José Cristino 77, Rio de Janeiro, RJ - 20921-400, Brazil*

[13]*Observatório Nacional, Rua Gal. José Cristino 77, Rio de Janeiro, RJ - 20921-400, Brazil*

[14]*Department of Astronomy, University of Illinois, 1002 W. Green Street, Urbana, IL 61801, USA*

[15]*National Center for Supercomputing Applications, 1205 West Clark St., Urbana, IL 61801, USA*

[16]*Institut de Ciències de l'Espai, IEEC-CSIC, Campus UAB, Facultat de Ciències, Torre C5 par-2, E-08193 Bellaterra, Barcelona, Spain*

[17]*Institut de Física d'Altes Energies (IFAE), The Barcelona Institute of Science and Technology, Campus UAB, E-08193, Spain*

[18]*George P. and Cynthia Woods Mitchell Institute for Fundamental Physics and Astronomy, and Department of Physics and Astronomy, Texas A&M University, College Station, TX 77843, USA*

[19]*Department of Physics, IIT Hyderabad, Kandi, Telangana 502285, India*

[20]*Department of Astronomy, University of Michigan, Ann Arbor, MI 48109, USA*

[21]*Department of Physics, University of Michigan, Ann Arbor, MI 48109, USA*

[22]*Kavli Institute for Cosmological Physics, University of Chicago, Chicago, IL 60637, USA*

[23]*Instituto de Fisica Teorica UAM/CSIC, Universidad Autonoma de Madrid, Cantoblanco E-28049 Madrid, Spain*

[24]*Department of Astronomy, University of California, Berkeley, 501 Campbell Hall, Berkeley, CA 94720, USA*

[25]*Lawrence Berkeley National Laboratory, 1 Cyclotron Road, Berkeley, CA 94720, USA*

[26]*Kavli Institute for Particle Astrophysics & Cosmology, PO Box 2450, Stanford University, Stanford, CA 94305, USA*

[27]*Department of Astronomy, University of Illinois, 1002 W. Green Street, Urbana, IL 61801, USA*

[28]*National Center for Supercomputing Applications, 1205 West Clark St., Urbana, IL 61801, USA*

[29]*Astronomy Department, University of Washington, Box 351580, Seattle, WA 98195, USA*

[30]*Cerro Tololo Inter-American Observatory, National Optical Astronomy Observatory, Casilla 603, La Serena, Chile*

[31]*Australian Astronomical Observatory, North Ryde, NSW 2113, Australia*
[32]*Departamento de Física Matemática, Instituto de Física, Universidade de São Paulo, CP 66318, CEP 05314-970 São Paulo, SP Brazil*
[33]*Department of Astrophysical Sciences, Princeton University, Peyton Hall, Princeton, NJ 08544, USA*
[34]*Institució Catalana de Recerca i Estudis Avançats, E-08010 Barcelona, Spain*
[35]*Jet Propulsion Laboratory, California Institute of Technology, 4800 Oak Grove Dr., Pasadena, CA 91109, USA*
[36]*Department of Physics and Astronomy, Pevensey Building, University of Sussex, Brighton BN1 9QH, UK*

[37]*Centro de Investigaciones Energéticas, Medioambientales y Tecnológicas (CIEMAT), E-28040 Madrid, Spain*
[38]*Universidade Federal do ABC, Centro de Ciências Naturais e Humanas, Av. dos Estados, 5001, Santo André, SP 09210-580, Brazil*
[39]*Computer Science and Mathematics Division, Oak Ridge National Laboratory, Oak Ridge, TN 37831, USA*

This paper has been typeset from a TEX/LATEX file prepared by the author.